# Coherent interaction of orthogonal polarization modes in a photonic crystal nanofiber cavity

Check for updates

# Coherent interaction of orthogonal polarization modes in a photonic crystal nanofiber cavity

JAMEESH KELOTH,[1] KALI P. NAYAK,[1,*] JIE WANG,[1] MAKOTO MORINAGA,[2] AND KOHZO HAKUTA[1]

[1]*Centre for Photonic Innovations, University of Electro-Communications, Chofu, Tokyo 1828585, Japan*
[2]*Institute of Laser Science, University of Electro-Communications, Chofu, Tokyo 1828585, Japan*
*\*kali@cpi.uec.ac.jp*

**Abstract:** We show that coherent interaction between two sets of multiple resonances leads to exotic resonant effects, such as Fano-type resonances, optical analogue of electro-magnetically induced transparency, and avoided crossing between modes, under different coupling regimes. We experimentally demonstrate such resonant effects in a photonic crystal nanofiber cavity using two sets of cavity modes with orthogonal polarizations. The interaction between the modes arises due to intra-cavity polarization mixing. The observed line shapes are reproduced using a multiple-mode interaction model. Such spectral characteristics may further enhance the capabilities of the nanofiber cavity as a fiber-in-line platform for nanophotonics and quantum photonics applications.

## 1. Introduction

Coherent interaction of resonances has been a fundamental area of interest and has enabled new ways to control light and matter. Exotic resonant effects such as Fano-type resonances, electro-magnetically induced transparency (EIT) and avoided crossing phenomena have been extensively investigated in atomic and molecular systems for several decades. In recent years, photonic analogue of such resonant effects has gained a broader attention. Fano-type resonances in various nanophotonic structures [1–6] have been demonstrated. Along with Fano-type resonances, other resonant effects such as avoided crossing and photonic analogue of EIT in various nanophotonic systems have been a hot topic of photonics research for a decade [7–9]. In particular, the sharp and narrow spectral features of such resonances have opened innovative prospects for applications like sensing [10–12], slow-light generation [13], nanolasers [14] and all-optical switching [15, 16].

Recently, Limonov *et al.* [2] have reviewed all such exotic effects in photonic structures and have shown that all the different effects can be easily explained as special cases of a two-mode interference model. Using this approach, interaction of single cavity mode with another single cavity mode or continuum (infinitely broad cavity mode) can be explained. However, for a cavity with multiple resonances, such an approach is only valid when the width of the resonances are much smaller than the free spectral range ($FSR$) of the cavity. In this context, extension of the model to explain the interaction of two sets of multiple resonances will be a more general approach and will be essential for various photonic systems [17, 18].

In recent years, tapered optical fibers with subwavelength diameter waist, known as optical nanofibers, have been a promising platform for nanophotonics [19, 20] and quantum photonics [21, 22]. The key features of the technique, are the strong field confinement [22] and efficient interaction with the surrounding medium [23] in a fiber-in-line platform. Moreover, the complex polarization properties of the nanofiber guided modes have led to the demonstration of chiral light-matter interactions [24]. The capabilities of the nanofiber technique can be further enhanced by implementing resonant photonic effects. In this context, high quality nanofiber cavities have been realized by inscribing photonic crystal (PhC) structures on an optical nanofiber using femtosecond

laser ablation technique [25–28]. Such nanofiber cavities have opened unique prospects for cavity quantum electrodynamics (cQED) and quantum photonics applications [26, 28].

One key feature of these PhC structures is that periodic array of nanocraters are formed on one side of the nanofiber, breaking the cylindrical symmetry of the nanofiber. As a result, these PhC structures are highly birefringent and have polarization dependent reflection bands leading to two orthogonal sets of polarization modes for the nanofiber cavity.

In this article, we demonstrate that exotic resonant effects such as Fano-type resonances, optical analogue of EIT and avoided crossing between modes, can be realized in a PhC nanofiber cavity by exploiting its polarization properties. We show that such spectral features originate due to the coherent interaction between two sets of cavity modes with orthogonal polarizations. Such interaction arises due to the intra-cavity polarization mixing. The observed line shapes are reproduced using a multiple-mode interference model under different coupling regimes. Such spectral characteristics combined with the capabilities of a nanofiber cavity, may open new avenues for nanophotonics and quantum photonics applications.

The article is organized as follows. In Section 2, we formulate the reflection and transmission coefficients of a cavity using a multiple-mode interference model. In Section 3, we present the experimental system, observations and analyze the observations using the model discussed in Section 2. In Section 4, we present the mechanism of polarization mixing. In Section 5, we present a brief discussion on the obtained results. Section 6 presents the summary and outlook of the work.
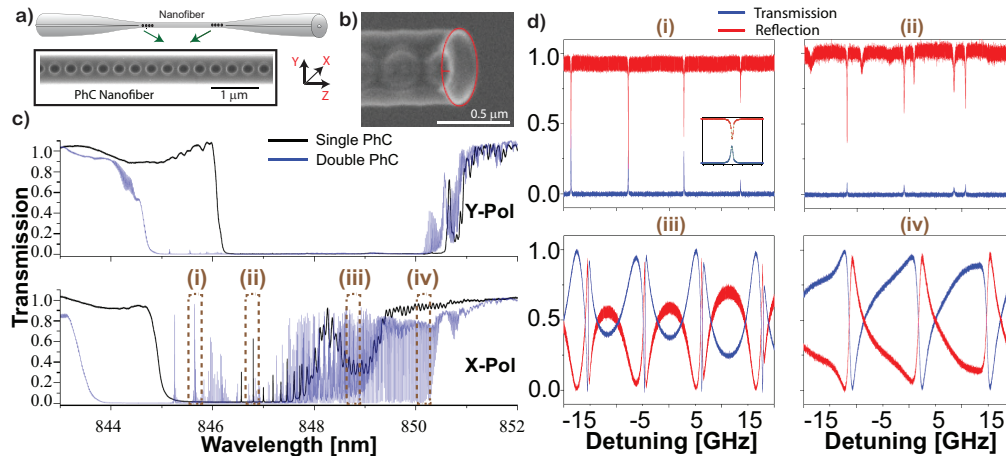


Fig. 1. (a) Schematic diagram of the PhC nanofiber cavity. The inset shows the SEM image of a typical section of the PhC nanofiber. (b) The SEM image showing the cross-sectional view of the PhC structure at a nanocrater position. (c) The transmission spectra of the nanofiber sample after the fabrication of the first (black traces) and second (blue traces) PhC, measured for Y-pol (upper panel) and X-pol (lower panel). (d) The expanded transmission (blue traces) and reflection (red traces) spectra of the nanofiber cavity for the X-pol, measured at four different regions (i), (ii), (iii) and (iv) marked by the dashed boxes in the lower panel of (c). The inset of panel (i) shows a single mode in region (i).

## 2. Theoretical model

In order to understand the coupling of the modes in a cavity, we adopt a multiple-mode interference model. We consider two sets of cavity modes having orthogonal polarizations, X- and Y-pol. $c_x^p$ and $c_y^q$ represent the cavity field amplitudes of the $p^{th}$ and $q^{th}$ modes of the X- and Y-pol cavities, respectively. The cavity modes $c_x^p$ and $c_y^q$ can be independently excited using the input fields

$a_x^{in}$ and $a_y^{in}$ and can decay out with a rate determined by the linewidths $\kappa_x^p$ and $\kappa_y^q$, respectively. We assume that in a finite spectral region, the decay rates of all X- and Y-pol modes are equal and are given as $\kappa_x$ and $\kappa_y$, respectively. It should be noted that $\kappa_x$ and $\kappa_y$ are the total decay rates and are given by $\kappa_x = \kappa_x^c + \kappa_x^s$ and $\kappa_y = \kappa_y^c + \kappa_y^s$. $\kappa_x^c = \kappa_x^i + \kappa_x^o$ and $\kappa_y^c = \kappa_y^i + \kappa_y^o$ are the total out-coupling rates where $(\kappa_x^i, \kappa_y^i)$ and $(\kappa_x^o, \kappa_y^o)$ are the out-coupling rates of the input and output mirrors, respectively. $\kappa_x^s$ and $\kappa_y^s$ are the loss rates due to scattering, for the respective cavity modes. By introducing a coherent interaction between the two sets of cavity modes, each cavity mode in one set, interferes and exchanges energy with the other set of cavity modes at a rate defined by the interaction strength $g$. The temporal dynamics of the field amplitudes can be represented by the coupled-mode equations as follows [17, 18]

$$\frac{dc_x^p}{dt} = -\frac{\kappa_x}{2}c_x - i\Delta_x^p c_x^p + \sqrt{\kappa_x^i}a_x^{in} - igc_y \tag{1}$$

$$\frac{dc_y^q}{dt} = -\frac{\kappa_y}{2}c_y - i\Delta_y^q c_y^q + \sqrt{\kappa_y^i}a_y^{in} - igc_x, \tag{2}$$

where $\Delta_x^p$ and $\Delta_y^q$ are the detunings of the corresponding modes from the excitation laser frequency, respectively. $c_x$ and $c_y$ are the coherent sum of the field amplitudes for X- and Y-pol cavities and are given as $c_x = \sum_p (-1)^p c_x^p$ and $c_y = \sum_q (-1)^q c_y^q$. The coefficients $(-1)^p$ and $(-1)^q$ represent the phase relation between the consecutive modes, *i.e.* symmetric and anti-symmetric modes. It should be noted that each set of polarization modes not only interacts with the orthogonal counterpart, but also with each other via the reservoir dynamics [17, 18].

We denote the output fields in the reflection and transmission side by $(a_x^{out}, a_y^{out})$ and $(b_x^{out}, b_y^{out})$ for (X-pol,Y-pol), respectively. The input and output fields can be related to the intra-cavity fields using the following boundary conditions [17, 18] ,

$$a_x^{in} + a_x^{out} = \sqrt{\kappa_x^i}c_x, \qquad b_x^{out} = \sqrt{\kappa_x^o}c_x, \tag{3}$$

$$a_y^{in} + a_y^{out} = \sqrt{\kappa_y^i}c_y, \qquad b_y^{out} = \sqrt{\kappa_y^o}c_y \tag{4}$$

We solve the coupled-mode equations under the steady-state regime assuming that the cavity is excited with only X-pol *i.e.* ($a_x^{in} = 1$ and $a_y^{in} = 0$). Then the reflection ($r_x = a_x^{out}/a_x^{in}, r_y = a_y^{out}/a_x^{in}$) and transmission ($t_x = b_x^{out}/a_x^{in}, t_y = b_y^{out}/a_x^{in}$) coefficients for (X-pol,Y-pol), respectively, can be obtained as

$$t_x = \frac{\sqrt{\kappa_x^i}\sqrt{\kappa_x^o}(\frac{\kappa_y}{2} + i\tilde{\Delta}_y)}{(\frac{\kappa_x}{2} + i\tilde{\Delta}_x)(\frac{\kappa_y}{2} + i\tilde{\Delta}_y) + g^2} \tag{5}$$

$$r_x = \frac{\kappa_x^i(\frac{\kappa_y}{2} + i\tilde{\Delta}_y)}{(\frac{\kappa_x}{2} + i\tilde{\Delta}_x)(\frac{\kappa_y}{2} + i\tilde{\Delta}_y) + g^2} - 1. \tag{6}$$

$$t_y = \frac{-ig\sqrt{\kappa_x^i}\sqrt{\kappa_y^o}}{(\frac{\kappa_x}{2} + i\tilde{\Delta}_x)(\frac{\kappa_y}{2} + i\tilde{\Delta}_y) + g^2} \tag{7}$$

$$r_y = \frac{-ig\sqrt{\kappa_x^i}\sqrt{\kappa_y^i}}{(\frac{\kappa_x}{2} + i\tilde{\Delta}_x)(\frac{\kappa_y}{2} + i\tilde{\Delta}_y) + g^2} \tag{8}$$

where

$$\frac{1}{\tilde{\Delta}_x} = \sum_p \frac{(-1)^p}{\Delta_x^p} = \sum_{p'=-n}^{p'=n} \frac{(-1)^{p'}}{\Delta_x^0 + p'FSR_x} \tag{9}$$

$$\frac{1}{\tilde{\Delta}_y} = \sum_q \frac{(-1)^q}{\Delta_x^q} = \sum_{q'=-n}^{q'=n} \frac{(-1)^{q'}}{\Delta_y^0 + q'FSR_y} \tag{10}$$

where $\Delta_x^0$ and $\Delta_y^0$ are the detunings of the two nearest modes of interest. The $FSR_x$ and $FSR_y$ represent the free spectral range for the X- and Y-pol cavities, respectively. $n$ is the number of modes considered on either sides of the modes of interest. The total intensity transmission and reflection of the cavity is then given by $T = |t_x|^2 + |t_y|^2$ and $R = |r_x|^2 + |r_y|^2$, respectively. Similarly, one can derive the total transmission and reflection for the case when the cavity is excited with only Y-pol *i.e.* ($a_x^{in} = 0$ and $a_y^{in} = 1$).

It should be noted that the characteristics of the line shapes are mainly determined by the linewidths of the nearest modes and the detuning between them. However the effect of the other modes are not negligible when the linewidths of the modes are comparable to the $FSR$ of the corresponding cavity. There are mainly two different coupling regimes. One is weak coupling regime, *i.e.* when $g$ is smaller than decay rate of one set of the modes ($\kappa_x \gg 2g$ or $\kappa_y \gg 2g$) and the other is strong coupling regime, *i.e.* when $g$ is larger than the decay rates of both the sets of modes ($\kappa_x, \kappa_y \ll 2g$).

Some peculiar effects occur in the weak coupling regime, when $\kappa_x$ and $\kappa_y$ have different values producing narrow and broad resonances. When the resonances of the two nearest modes of orthogonal polarizations have a finite detuning, $\Delta_{xy}^0 = \Delta_y^0 - \Delta_x^0 \neq 0$, the phase of the narrower mode changes by $\pi$ across its resonance while the phase of the broader mode varies slowly. This leads to formation of constructive and destructive interference on either side of the narrow mode resonance, resulting in asymmetric line shapes resembling Fano-type line shapes. Under the same weak coupling regime, when $\Delta_{xy}^0 \sim 0$, the asymmetry in the line shape vanishes. This results in the formation of a transmission window in the reflection spectrum, illustrating the optical analogue of EIT. One extreme case of the weak coupling regime, is when the linewidth of the broader mode is much bigger than the $FSR$ of the cavity. In this case, the broader mode effectively acts as a continuum which interferes with the narrow mode with orthogonal polarization, illustrating the Fano resonance condition.

In the strong coupling regime, *i.e.* $2g \gg \kappa_x, \kappa_y$, along with the spectral shapes, the eigenfrequencies of the coupled modes are seriously modified. One can derive the eigenfrequencies of the coupled modes from the steady-state solutions of the coupled mode equations [2]. Assuming $|\kappa_x - \kappa_y| \ll g$, the modified eigenfrequencies ($\omega_\pm$) are given by

$$\omega_\pm = \frac{\Delta_x^0 + \Delta_y^0}{2} \pm \sqrt{(\frac{\Delta_x^0 - \Delta_y^0}{2})^2 + g^2}. \tag{11}$$

It may be seen from the above equation that when $|\Delta_x^0 - \Delta_y^0| \gg g$, the frequency spacing between the coupled modes is similar to that of the uncoupled modes, $|\Delta_x^0 - \Delta_y^0|$. However, when the $|\Delta_x^0 - \Delta_y^0| \sim 0$, the frequency spacing between the coupled modes will be $\sim 2g$. These spectral features illustrate the avoided crossing between two strongly coupled modes.

## 3. Experimental observations

We experimentally demonstrate the above discussed spectral features using a photonic crystal nanofiber cavity. A schematic diagram of the PhC nanofiber cavity is shown in Fig. 1(a). The nanofiber is located at the waist of a tapered single mode optical fiber. The typical diameter and length of the nanofiber waist used for this experiment is 500 nm and 15 mm, respectively. The nanofiber cavity is formed by fabricating two PhC structures on the optical nanofiber separated by a length, $L = 12$ mm. The PhC structures are fabricated using femtosecond laser ablation technique [25–27]. The inset of Fig. 1(a) shows the scanning electron microscope (SEM) image of a typical part of the PhC structure. It may be seen that periodic nanocraters are formed on the

nanofiber. The periodic nanocraters on the nanofiber induce strong modulation of the refractive index and act as a Bragg reflector for the nanofiber guided modes. We define a coordinate system as depicted in Fig. 1(a). The Z-axis denotes the nanofiber axis and the X-axis marks the azimuthal position of the nanocraters on the nanofiber.

A cross-sectional view of the PhC structure at the nanocrater position is shown in Fig. 1(b). It may be seen that the nanocrater is formed on one side of the nanofiber along the X-axis. As a result, the cylindrical symmetry of the nanofiber is broken. This will induce a difference between the effective indices ($n_{eff}$) of X- and Y-polarized guided modes. Therefore the PhC nanofiber can be highly birefringent.

The birefringence of the PhC nanofiber is further clarified from the spectral characteristics. The transmission and reflection spectra are measured using a tunable, narrow linewidth diode laser (Newport TLB6700), as in Ref. [28]. The black traces in lower and upper panels in the Fig. 1(c), show the transmission spectra measured after the fabrication of a single PhC structure, for two orthogonal polarizations, X- and Y-pol, respectively. It may be seen that wide stop bands (reflection bands) with a width of 3-4 nm are formed in the transmission spectra of both polarizations, where the guided light is strongly Bragg reflected. Also it may be clearly seen that the center of the reflection band for the X-pol is blue-shifted by ∼2 nm compared to that for the Y-pol. This may correspond to an effective index difference ($\Delta n_{eff}$) of 0.25% between the two polarizations. Thus the PhC nanofiber is highly birefringent and acts as a polarization dependent Bragg mirror.

The blue traces in Fig. 1(c), show the transmission spectra for the X- and Y-pol after the fabrication of the second PhC. It may be seen that the widths of the stop bands increased and sharp cavity modes appeared. The four panels of Fig. 1(d), show the measured reflection and transmission spectra for the X-pol at four regions of the stop band marked by the dashed boxes and denoted as (i), (ii), (iii) and (iv) in the lower panel of Fig. 1(c). As seen from the panel (i) of Fig. 1(d), equally spaced modes are observed with a frequency spacing of 11 GHz. This spacing well corresponds to the estimated $FSR (= c/(2n_{eff}L))$ of the cavity formed between the two PhC structures, where $c$ is the speed of light and $n_{eff} = 1.14$. Usual Lorentzian line shapes are observed in this region as shown in the inset of panel (i) of Fig. 1(d). The cavity modes are observed with high quality factors up to 10 million (FWHM = 34 MHz). Such nanofiber cavities along with the key features of nanofiber technique, such as the strong field confinement [22] and efficient interaction with the surrounding medium [23] in a fiber-in-line platform, have opened unique prospects for cQED and quantum photonics applications [26, 28].

Apart from the usual cavity modes, some peculiar spectral characteristics are also observed. In the region (ii), double-mode features are observed within one $FSR$. In the region (iii), the cavity is partly transmitting and partly reflecting. The cavity modes show peculiar features where narrow peaks (dips) appear within broad reflection dips (transmission peaks), respectively. These spectral features resemble the optical analogue of EIT. In the region (iv), the cavity is mostly transmitting and the observed cavity modes are inverted, appearing as transmission dips and reflection peaks. Moreover the line shapes are highly asymmetric resembling Fano-type resonances.

The spectral features described above can be understood as a result of coupling between the two sets of polarization modes of the cavity. It may be clearly seen that for the X-pol, the region (iv) is completely out of the stop band of the first PhC. Therefore, the reflection of the X-pol from the first PhC is negligible in this spectral region, which discards the possibility for the formation of narrow cavity modes for the X-pol. However, in this region the Y-pol is still strongly reflected from both the PhC, which may lead to formation of narrow cavity modes. So the narrow spectral features observed for the X-pol can only be explained as a result of coupling with the Y-pol modes. In the preceding section, we analyze the different spectral features using the multi-mode interference model.
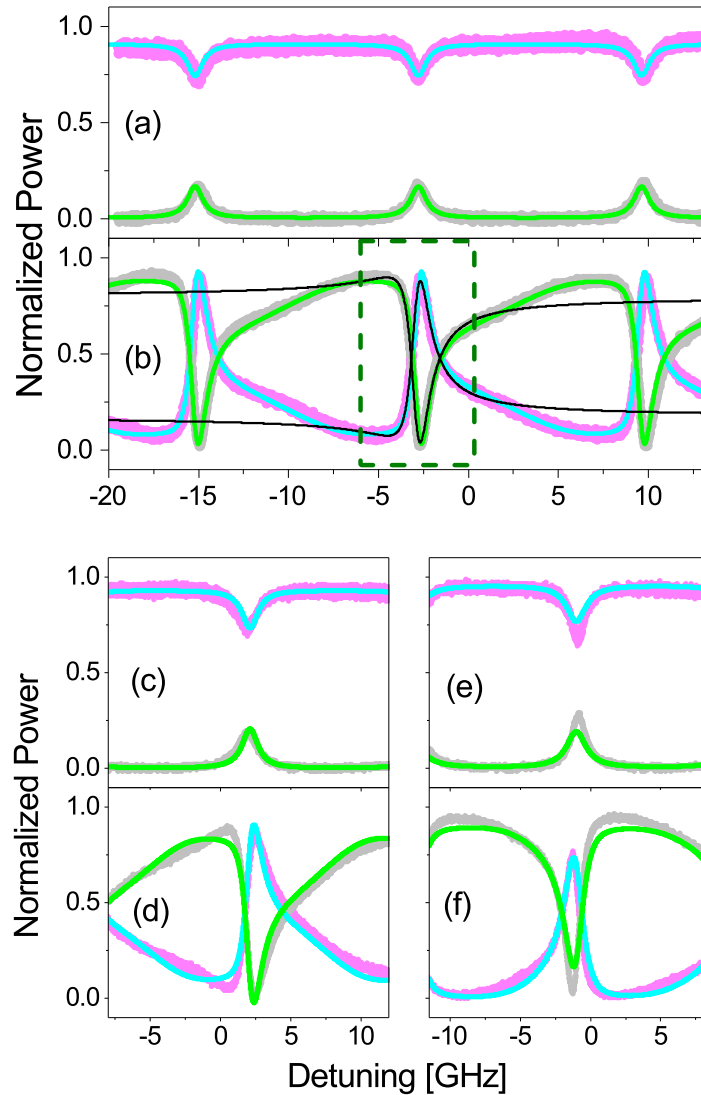
### 3.1. Fano-type resonances



Fig. 2. Typical spectral line shapes observed in region (iv). (a) and (b) show the reflection (magenta traces) and transmission (gray traces) spectra measured when the cavity is excited with Y-pol and the corresponding line shapes when the cavity is excited with X-pol, respectively. The green (transmission) and cyan (reflection) traces show the fitted curves using the multiple-mode interference model. The black traces show the fitted curves using the phenomenological Fano line shape formula for data points within the region marked by the dashed lines. (c,d) and (e,f) show two more sets of spectra measured in the same region.

As described in the previous section, Fano-type resonances are observed for the X-pol in the region (iv) as indicated in Fig. 1(c). Figures 2(a) and 2(b) show the line shapes measured in this region when the cavity is excited with Y-pol and X-pol, respectively. The magenta and gray traces show the line shapes measured in the reflection and transmission ports of the cavity,

respectively. It may be clearly seen that for Y-pol (Fig. 2(a)), the cavity is mostly reflecting and cavity modes appear as reflection dips and transmission peaks with rather symmetric Lorentzian line shapes. However, when the input polarization is changed to X-pol (Fig. 2(b)), the cavity is mostly transmitting and cavity modes appear as transmission dips and reflection peaks with asymmetric line shapes resembling Fano-type resonances. We fit the observed line shapes using the theoretical model discussed above. Here we consider, both X- and Y-pol cavities are symmetric *i.e.*, $\kappa_x^i = \kappa_x^o = \kappa_x^c/2$ and $\kappa_y^i = \kappa_y^o = \kappa_y^c/2$. For the fitting, we consider $n = 20$, *i.e.* 20 consecutive modes on either side of the central mode. This is a good approximation considering the $FSR$ and width of the broad mode. To find the best fit we adopt a nonlinear least square method and minimize the sum of the squared residuals. The fitted curves are shown as cyan (reflection) and green (transmission) traces. It may be seen that the theoretical model can clearly reproduce the line shapes for both the polarizations with the same fitting parameters. The estimated parameters ($\kappa_x^c$, $\kappa_y^c$, $FSR_x$, $\delta FSR = FSR_y - FSR_x$, $\Delta_{xy}^0 = \Delta_y^0 - \Delta_x^0$ and $g$) are summarized in the first row of Table 1. It should be noted that the estimated $\kappa_x^s$ and $\kappa_y^s$ values are $\sim 0$ for the data shown.

We have analyzed two more sets of data measured in this region using the model discussed, as shown in Figs. 2(c) and 2(d) and 2(e) and 2(f). The estimated parameters are summarized in the second and third row of Table 1. From the fittings, it is clear that in this region, $\kappa_x$ is much larger than the $FSR_x$, and the modes for the X-pol effectively act as continuum. On the other hand, the modes for the Y-pol possess linewidths ($\kappa_y$) of 300-380 MHz. The coupling rate $g$ is in the range of 2.5 - 3.3 GHz. As a result of the coupling between the two polarization modes, Fano-type asymmetric resonances appear when the cavity is excited with X-pol and effectively broadened Lorentzian line shapes appear when cavity is excited with Y-pol. The Lorentzian linewidths estimated for the modes shown in Fig. 2(a) is $\sim 2$ GHz while the estimated width of the uncoupled Y-pol mode is 300 MHz.

Table 1. Estimated fitting parameters in GHz unit.

| Region | $\kappa_x^c$ | $\kappa_x^s$ | $\kappa_y^c$ | $\kappa_y^s$ | $\Delta_{xy}^0$ | $FSR_x$ | $\delta FSR$ | $g$ | Fig. No. |
|---|---|---|---|---|---|---|---|---|---|
|  | 18.27 | - | 0.300 | - | -9.30 | 12.43 | 0.02 | 2.52 | 2(a),2(b) |
| iv | 15.98 | - | 0.380 | - | -8.80 | 12.96 | 0.05 | 2.68 | 2(c),2(d) |
|  | 30.05 | - | 0.320 | - | 5.60 | 10.68 | 1.13 | 3.27 | 2(e),2(f) |
|  | 7.50 | 0.530 | 0.005 | 0.101 | 0.83 | 10.70 | 0.70 | 1.06 | 3(a) |
| iii | 7.80 | 0.072 | 0.016 | 0.053 | -3.05 | - | - | 0.93 | 3(b) |
|  | 7.75 | 0.480 | 0.010 | 0.100 | 1.36 | - | - | 1.06 | 3(c) |
| ii | 0.32 | 0.007 | 0.005 | 0.013 | -0.80 | 12.10 | 3.48 | 1.52 | 4 |

## 3.2. EIT-like line shapes

As described in the previous subsection, the $\kappa_x$ values in the region (iv) are much larger than the $FSR_x$, so it is difficult to visualize the two polarization modes. However, in the region (iii) the X-pol has finite reflection from both the PhCs and the linewidths of the X-pol modes are comparable to the $FSR_x$ of the cavity while the Y-pol modes have much narrow linewidths. As a result, the two-mode interference effect can be clearly visualized. The magenta (gray) traces in Fig. 3, show the three typical reflection (transmission) spectra observed in this region, when the cavity is excited with X-pol. Figure 3(a) shows three consecutive modes measured in this region. It may be clearly seen that a broad reflection (transmission) dip (peak) with a narrow
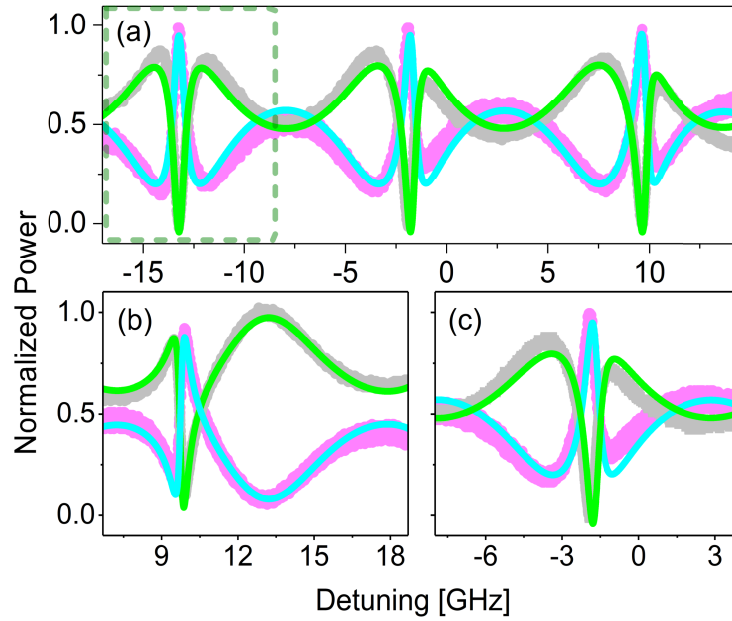
Fig. 3. Magenta and gray traces show the experimentally measured reflection and transmission spectra in the region (iii) when the cavity is excited with X-pol. The cyan (reflection) and green (transmission) traces show the theoretical fits using the multiple-mode interference model. (a) shows three consecutive modes measured in this region. The dashed box shows a case when the detuning between the polarization modes is ∼ 0.83 GHz. (b) and (c) show the two cases when the detunings between the polarization modes are -3.05 and 1.36 GHz, respectively.

transmission (reflection) window is observed. The transmission (reflection) window looks rather symmetric when it appears at the center of the reflection dip (transmission peak) as marked by the dashed box in Fig. 3(a). It may be seen that for the consecutive modes the position of the transmission (reflection) window is gradually shifting towards the higher frequency side of the broad mode. As shown in Figs. 3(b) and 3(c), when the transmission (reflection) window is shifted to either side of the reflection dip (transmission peak), it shows asymmetric profile. Such spectral characteristics illustrate the optical analogue of EIT and is understood from the coupling between the two polarization modes.

We fit the observed line shapes using the model described in Section 2. In this region also, we consider both X- and Y-pol cavities are symmetric *i.e.*, $\kappa_x^i = \kappa_x^o = \kappa_x^c/2$ and $\kappa_y^i = \kappa_y^o = \kappa_y^c/2$. The fitted curves are shown by the cyan and green traces for reflection and transmission, respectively. The estimated fitting parameters ($\kappa_x^c, \kappa_y^c, \kappa_x^s, \kappa_y^s, \Delta_{xy}^0, g$) are summarized in Table 1. From the estimated parameters, it may be seen that the $\kappa_x$ and $\kappa_y$ values are in the range of 8.0 - 8.5 GHz and 0.06 - 0.11 GHz, respectively. The coupling rate $g$ is ∼ 1 GHz. The estimated $FSR_x$ and $\delta FSR$ values are 10.7 and 0.70 GHz, respectively. As a result of the finite difference in the $FSR$ values, the detuning between the X- and Y-pol modes changes gradually for the consecutive modes. The key difference between the line shapes arises due to the different detuning between the two nearest modes. The dashed box shows a case when the detuning between the nearest modes is ∼ 0.83 GHz. Figures 3(b) and 3(c) show the two cases when the detunings between the nearest modes are -3.05 and 1.36 GHz, respectively. The estimated $\kappa_x^s$ and $\kappa_y^s$ values are in the range of 0.07- 0.53 GHz and 0.053 - 0.101 GHz, respectively. Although the $\kappa_x^s$ values are not

zero, but small compared the $\kappa_x$. So the effect of the $\kappa_x^s$ on the line shape is negligible. On the other hand, $\kappa_y^s$ is comparable to $\kappa_y$ and as a result, the cavity modes were not observable when the cavity was excited with Y-pol.
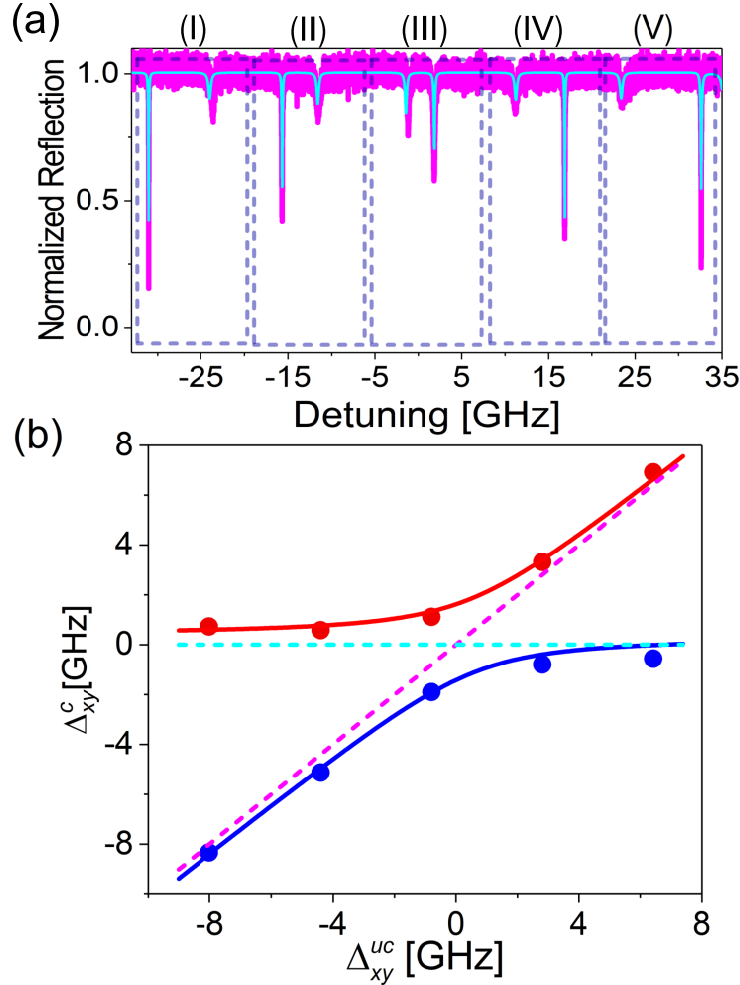
### 3.3. Avoided crossing between cavity modes



Fig. 4. (a) Magenta trace shows the experimentally measured reflection spectra in the region (ii), when the cavity is excited with X-pol and cyan trace show the theoretical fit using the multiple-mode interference model. (b) Red and blue dots show the detuning of the modified Y- and X-pol modes with respect to the uncoupled Y-pol mode. The horizontal axis represents the detuning between the uncoupled modes. Whereas the vertical axis denotes the detunings of the coupled modes with respect to the uncoupled mode of Y-pol. Magenta and cyan dashed lines represent the detuning between the uncoupled modes. The red and blue traces show the theoretical fit to the measured detunings of the coupled modes.

The Fano- and EIT-like line shapes presented in the previous subsections correspond to the weak coupling regime. This is marked from the fact that $\kappa_x \gg 2g$, in the regions (iii) and (iv). However, in the region (ii) both the polarizations are strongly reflected from both the PhCs. This may lead to strong coupling regime, $(\kappa_x, \kappa_y) \ll 2g$. Figure 4(a) shows a typical part of the

reflection spectrum for X-pol observed in this region. It should be noted that, in this region, the transmission spectrum was not observable. For convenience of presentation, we divide the spectral region into 5 panels, each with a width of $\sim FSR_x$. In each panel, peculiar double-mode spectral features are observed in this region. In the panel (I), there are two modes. One is a sharp and strong reflection dip and the other is a tiny and broader dip which appears at 8 GHz higher frequency detuning. In the panel (II), the two modes get closer to each other with a slight modification in the line shapes. In the panel (III) the two modes are much closer and have similar spectral features. In the subsequent panels the spectral features are reversed with the narrow mode gradually moving apart from the broad mode towards the higher detuning side. These spectral features illustrate the avoided crossing phenomenon when the two strongly coupled modes cross each other.

In order to get further insight about the frequency spacing between the uncoupled modes in each panel, we fit the data using the multiple-mode interference model. The fitted curve is shown by the cyan trace in Fig. 4(a). In this region, we were able to reproduce the results by considering one-sided cavity *i.e.*, $\kappa_x^i = \kappa_x^c$, $\kappa_y^i = \kappa_y^c$, $\kappa_x^o = 0$ and $\kappa_y^o = 0$. The fitting parameters are summarized in Table 1. The $\kappa_x$, $\kappa_y$ and $g$ are estimated to be 327 MHz, 18 MHz and 1.52 GHz, respectively. From the fit, we estimate the $FSR_x$ and $\delta FSR$ values as 12.1 GHz and 3.48 GHz respectively. As a result of the finite difference in the $FSR$ values, the detuning between the X- and Y-pol modes (uncoupled modes) changes gradually for the consecutive modes. The scattering rate for X- and Y-pol cavities, $\kappa_x^s$ and $\kappa_y^s$, are estimated as 7 and 13 MHz, respectively. Therefore the effect of the scattering loss on the observed lineshapes are not negligible and it is also essential to reproduce the on-resonance reflection values.

We re-define the frequency detunings of the uncoupled and coupled modes with respect to the frequency position of the uncoupled mode of Y-pol. The measured values for coupled resonances are plotted in Fig. 4(b) as red and blue dots. The vertical axis represents the detunings ($\Delta_{xy}^c$) of the coupled modes with respect to the uncoupled mode of Y-pol. Whereas the horizontal axis denotes the detunings ($\Delta_{xy}^{uc}$) between the uncoupled modes for each panel. The frequency detuning of the uncoupled modes for X- and Y-pol are indicated by the magenta and cyan dashed lines. It may be seen that although the uncoupled modes get closer and cross each other towards panel (III), the coupled modes are still separated by 3 GHz. We fit the modified eigenvalues using Eq. (11). The fitted curves are shown by blue and red traces in Fig. 4(b). From the fitting, we estimate the $g$-value to be $1.5 \pm 0.11$ GHz.
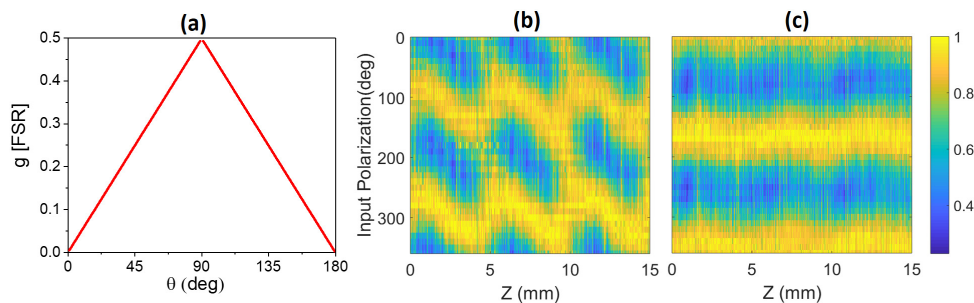
## 4. Mechanism of polarization mixing



Fig. 5. (a) Dependency of $g$ on the total single-pass polarization rotation ($\theta$). The vertical axis is normalized to the $FSR$ of the cavity. (b) and (c) The measured intensity pattern of the light scattered by the nanofiber segment as a function of the input polarization of the guided light and the distance ($Z$) along the fiber axis for sample (i) and (ii) respectively. Colorbar represents the normalized intensity.

The interference between two sets of orthogonal polarization modes is possible only when there is a finite intra-cavity polarization mixing. The polarization mixing can occur due to a finite rotation of polarization between the two PhCs or a finite angle between the birefringent axes of the two PhCs. Using a transfer matrix method [29], we have theoretically investigated the dependency of $g$ on the intra-cavity polarization rotation. A similar formalism can be found in Ref. [30]. The dependency of $g$ on the total single-pass rotation ($\theta$), is plotted in Fig. 5(a). It should be noted that, here $g$ is normalized to the $FSR$ of the cavity. A periodic dependency of $g$ on $\theta$ is observed with a period of 180°. A maximum coupling rate ($g = FSR/2$) is observed for $\theta = 90°$. This suggests that for the presented nanofiber cavity ($FSR \sim 11$ GHz), even a rotation of $\theta \sim 16°$ will induce a coupling rate of 1 GHz.

Next we discuss the physical origin of the polarization mixing. The fabrication process ensures a minimum relative mismatch between the birefringence axes of the two PhCs. Therefore the main mechanism behind polarization mixing is the intra-cavity polarization rotation. The polarization rotation can occur due to a combined effect of the birefringence properties of the PhC structures and the intra-cavity nanofiber segment. A finite mismatch between the birefringence axes of the nanofiber segment and PhCs, will lead to polarization rotation.

As described in the context of Fig. 1(c), the PhC structure is highly birefringent, with $\Delta n_{eff} \sim 0.25\%$. From this, a maximum polarization rotation ($\Delta\theta/\Delta z = \pi\Delta n_{eff}/\lambda$) can be estimated as $\sim 603°$/mm, where $\lambda = 850$ nm is the wavelength of light. Due to the distributed nature of the Bragg reflection, the PhCs not only act as mirrors, but also as retardation plates, inducing polarization rotation. The amount of rotation will depend on the angle of input polarization with respect to the birefringence axis and the penetration length into the PhC mirror. Moreover different wavelengths across the stop band may have different penetration lengths resulting in wavelength dependent variation of total intra-cavity polarization rotation.

The nanofiber segment between the two PhCs can also have birefringence arising due to the ellipticity of the nanofiber cross-section. We have experimentally measured the polarization rotation in the nanofiber segment by observing the angular distribution of the Rayleigh scattered light from the nanofiber [31]. The intensity pattern of the light scattered by the nanofiber, is measured along the length of the nanofiber by varying the input polarization of the guided light. The scattered light is observed using a CCD camera aligned perpendicular to the nanofiber axis and only the polarization component orthogonal to the nanofiber axis, is measured.

The 2D plots in Figs. 5(b) and 5(c) show the measurements carried out for two typical samples (i) and (ii), respectively. In the case of sample (i), the polarization rotation along the nanofiber is clearly observed. This is marked by the periodic modulation of the intensity pattern along the length of the nanofiber. From the measured spatial period of $\Lambda_p \sim 5$ mm along the length of the nanofiber, we estimate a maximum polarization rotation of $\Delta\theta/\Delta z = \pi/\Lambda_p \sim 36°$/mm. This may correspond to an effective refractive index difference of $\Delta n_{eff} \sim 0.017\%$ for two orthogonal polarizations. Using finite difference time domain simulations (FDTD Solutions, Lumerical Inc.), we have estimated that the measured $\Delta n_{eff}$ may correspond to an ellipticity of $\sim 0.21\%$ *i.e.* a diameter difference of ~1 nm. On the other hand for the sample (ii), we have observed only a small rotation of polarization over the entire length of the nanofiber segment, which is within the angular accuracy of 10°. We have fabricated PhC cavities on both sample (i) and sample (ii). The interference between the polarization modes is observed for both the cavities. The data presented in the previous section correspond to the sample (i).

## 5. Discussions

Table 1 summarizes the fitting parameters estimated for different regions. It is evident that the interaction dynamics between the two sets of cavity modes governs the different spectral features. Fano- and EIT-like line shapes are observed when the polarization modes couple weakly, *i.e.* $\kappa_x \gg 2g \gg \kappa_y$. When the two polarization modes satisfy the strong coupling condition, *i.e.*

$(\kappa_x, \kappa_y) \ll 2g$, avoided crossing of the two modes is observed.

The multiple-mode interference model is essential to faithfully reproduce the spectral features. In fact a two-mode interference model can explain the features only in a limited bandwidth region. Especially in the weak coupling regime when the linewidths of the broad modes are comparable to the $FSR$ and the adjacent modes are overlapping, such a model fails. On the other hand, it may be intriguing to fit the Fano-type line shapes shown in Fig. 2(b), using the phenomenological Fano line shape formula [1, 2] given by

$$y = \frac{1}{q^2 + 1} \frac{(q\kappa_{eff} + \omega)^2}{\kappa_{eff}^2 + \omega^2}, \tag{12}$$

where $\kappa_{eff}$ is the effective linewidth of the mode, $q$ is the Fano-parameter (asymmetry parameter) and $\omega$ is the frequency detuning. It should be noted that when the q-value is close to 1, the asymmetry is maximum and as the q-value becomes much greater than 1, the asymmetry reduces but the spectra are inverted. The black traces in Fig. 2(b) show the fittings using Eq. (12), for data points within the region marked by the dashed lines. From the fittings, we estimated the $q$-value to be 2.7 for Fig. 2(b). It may be seen that the above formula can reproduces the spectral features only in the central region. Whereas in the tail region the fitted curve clearly deviates from the observations. This is due to the contribution from the adjacent modes, which can only be explained considering the multiple-mode interference model.

As shown in Fig. 4(a), the model not only reproduces the eigenfrequencies but also can qualitatively predict the spectral shapes and the on-resonance reflection. It should be noted that, here the loss rate due to scattering plays an important role to predict line-shapes. This is due to the fact that in this region (region (ii)) the linewidths are much narrow and are mainly dominated by the scattering loss. However in the weak coupling regime (region (iii) and (iv)) the effect of scattering loss is negligible.

It can be seen from Table 1 that the estimated values for $g$ ranges from 0.9 to 3.3 GHz, for different regions across the stop band. This can be understood from the polarization rotation of 36°/mm in the intra-cavity nanofiber segment for the sample (i), as discussed in the previous section. On the other hand, for the cavity fabricated on sample (ii), we have observed a maximum $g$ value of $\sim$ 1 GHz, which corresponds to a $\sim$ 16° polarization rotation between the two PhCs. Although the measured polarization rotation for this sample is less than 10°, the combined effect of the small but finite rotation of polarization in the nanofiber segment and strong birefringence of the PhCs, may enhance the total polarization rotation to explain the observed $g$ values.

Based on these understandings, the line shapes can be designed according to the requirements of specific applications. The decay rates $\kappa_x$ and $\kappa_y$ can be controlled by selecting the appropriate spectral region. Whereas, the $g$ value can be controlled by varying total amount of polarization rotation between the two mirrors, by inducing a relative axial rotation of the PhC axes and controlling the birefringence of the nanofiber section.

## 6. Summary and outlook

We demonstrate that exotic photonic effects such as Fano-type resonances, optical analogue of EIT and avoided crossing between modes, can be realized in a photonic crystal nanofiber cavity by exploiting its polarization properties. We show that such spectral features originate due to the coherent interaction between two sets of multiple cavity modes with orthogonal polarizations. Such interaction arises due to the intra-cavity polarization mixing. The observed line shapes are reproduced using a multiple-mode interference model under different coupling regimes.

Such photonic effects are promising in realizing fine control of light in micro and nanophotonic structures. In particular, the unique properties of a nanofiber such as the strong field confinement and efficient interaction with the surrounding medium in a fiber-in-line platform, may further enhance the capabilities for new applications in nanophotonics and quantum photonics.

## References

1. A. E. Miroshnichenko, S. Flach, and Y. S. Kivshar, "Fano resonances in nanoscale structures," Rev. Mod. Phys. **82**, 2257–2298 (2010).
2. M. F. Limonov, M. V. Rybin, A. N. Poddubny, and Y. S. Kivshar, "Fano resonances in photonics," Nat. Photonics **11**, 543–554 (2017).
3. M. Galli, S. L. Portalupi, M. Belotti, L. C. Andreani, L. O'Faolain, and T. F. Krauss, "Light scattering and Fano resonances in high- Q photonic crystal nanocavities," Appl. Phys. Lett. **94**, 071101 (2009).
4. B. Li, Y. Xiao, C. Zou, Y. Liu, X. Jiang, Y Chen, Y. Li, and Q Gong, "Experimental observation of Fano resonance in a single whispering-gallery microresonator," Appl. Phys. Lett. **98**, 021116 (2011).
5. A. Chiba, H. Fujiwara, J. Hotta, S. Takeuchi, and K. Sasaki, "Fano resonance in a multimode tapered fiber coupled with a microspherical cavity," Appl. Phys. Lett. **86**, 261106 (2005).
6. S. Fan, "Sharp asymmetric line shapes in side-coupled waveguide-cavity systems," Appl. Phys. Lett. **80**, 908–910 (2002).
7. B. Peng, S. K. Ozdemir, W. Chen, F. Nori, and L. Yang, "What is and what is not electromagnetically induced transparency in whispering-gallery microcavities," Nat. Commun. **5**, 5082 (2014).
8. Y. Yang, I. I. Kravchenko, D. P. Briggs, and J. Valentine, "All-dielectric metasurface analogue of electromagnetically induced transparency," Nat. Commun. **5**, 5753 (2014).
9. S. Han, L. Cong, H. Lin, B. Xiao, H. Yang, and R. Singh, "Tunable electromagnetically induced transparency in coupled three-dimensional split-ring-resonator metamaterials," Sci. Rep. **6**, 20801 (2016).
10. B. Zeng, Y. Gao, and F. J. Bartoli, "Rapid and highly sensitive detection using Fano resonances in ultrathin plasmonic nanogratings," Appl. Phys. Lett. **105**, 161106 (2014).
11. N. Liu, T. Weiss, M. Mesch, L. Langguth, U. Eigenthaler, M. Hirscher, C. Sonnichsen, and H. Giessen, "Planar metamaterial analogue of electromagnetically induced transparency for plasmonic sensing," Nano Lett. **10**, 1103–1107 (2010).
12. Z. Dong, H. Liu, J. Cao, T. Li, S. Wang, S. Zhu, and X. Zhang, "Enhanced sensing performance by the plasmonic analog of electromagnetically induced transparency in active metamaterials," Appl. Phys. Lett. **97**, 114101 (2010).
13. K. Totsuka, N. Kobayashi, and M. Tomita, "Slow light in coupled-resonator-induced transparency," Phys. Rev. Lett. **98**, 213904 (2007).
14. Y. Yu, W. Xue, E. Semenova, K. Yvind, and J. Mørk, "Demonstration of a self-pulsing photonic crystal Fano laser," Nat. Photon. **11**, 81–85 (2017).
15. Y. Yu, M. Heuck, H. Hu, W. Xue, C. Peucheret, Y. Chen, L. K. Oxenløwe, K. Yvind, and J. Mørk, "Fano resonance control in a photonic crystal structure and its application to ultrafast switching," Appl. Phys. Lett. **105**, 061117 (2014).
16. L. Stern, M. Grajower, and U. Levy, "Fano resonances and all-optical switching in a resonantly coupled plasmonic atomic system," Nat. Commun. **5**, 4865 (2014).
17. C. Viviescas and G. Hackenbroich,"Field quantization for open optical cavities," Phys. Rev. A **67**, 013805 (2003).
18. J. M. Dobrindt and T. J. Kippenberg, "Theoretical analysis of mechanical displacement measurement using a multiple cavity mode transducer," Phys. Rev. Lett. **104**, 033901 (2010).
19. G. Brambilla, "Optical fibre nanowires and microwires: a review," J. Opt. A **12**, 043001 (2010).
20. L. Tong, F. Zi, X. Guo, and J. Lou,"Optical microfibers and nanofibers: a tutorial," Opt. Commun. **285**, 4641–4647 (2012).
21. P. Solano, J. A. Grover, J. E. Hoffman, S. Ravets, F. K. Fatemi, L. A. Orozco, and S. L. Rolston, "Optical nanofibers: a new platform for quantum optics," Advances In Atomic, Molecular, and Optical Physics **66**, 439 (2017).
22. K. P. Nayak, M. Sadgrove, R. Yalla, F. L. Kien, and K. Hakuta, "Nanofiber quantum photonics," J. Opt. **20**, 073001 (2018).
23. F. L. Kien, S. D. Gupta, V. I. Balykin, and K. Hakuta, "Spontaneous emission of a cesium atom near a nanofiber: efficient coupling of light to guided modes," Phys. Rev. A **72**, 032509 (2005).
24. P. Lodahl, S. Mahmoodian, S. Stobbe, A. Rauschenbeutel, P. Schneewiss, J. Volz, H. Pichler, and P. Zoller, "Chiral quantum optics," Nature **541,** 473–480 (2017).
25. K. P. Nayak and K. Hakuta, "Photonic crystal formation on optical nanofibers using femtosecond laser ablation technique," Opt. Express **21**, 2480–2490 (2013).

26. K. P. Nayak, P. Zhang, and K. Hakuta, "Optical nanofiber-based photonic crystal cavity," Opt. Lett. **39**, 232–235 (2014).
27. K. P. Nayak, J. Keloth, and K. Hakuta, "Fabrication of 1-D photonic crystal cavity on a nanofiber using femtosecond laser-induced ablation," J. Vis. Exp. **120**, e55136 (2017).
28. J. Keloth, K. P. Nayak, and K. Hakuta, "Fabrication of a centimeter-long cavity on a nanofiber for cavity quantum electrodynamics," Opt. Lett. **42**, 1003–1006 (2017).
29. H. A. Haus, *Waves and Fields in Optoelectronics* (Prentice Hall, 1984), Vol. 1.
30. K. Kolluru, S. Saha, and S. D. Gupta, "Cavity enhanced interference of orthogonal modes in a birefringent medium," Opt. Comm. **410**, 836–840 (2018).
31. E. Vetsch, S. T. Dawkins, R. Mitsch, D. Reitz, P. Schneeweiss, and A. Rauschenbeutel, "Nanofiber-based optical trapping of cold neutral atoms," IEEE J. Sel. Top. Quantum Electron. **18,** 1763–1770 (2012).